# Isolating Bandpass Filters Using Time-Modulated Resonators

Xiaohu Wu, *Member, IEEE*, Xiaoguang Liu, *Senior Member, IEEE*, Mark D. Hickle, *Member, IEEE*, Dimitrios Peroulis, *Fellow, IEEE*, Juan Sebastián Gómez-Díaz, *Senior Member, IEEE*, and Alejandro Álvarez Melcón, *Senior Member, IEEE*

***Abstract*— In this paper, we demonstrate, for the first time, an isolating bandpass filter with low-loss forward transmission and high reverse isolation by modulating its constituent resonators. To understand the operating principle behind the device, we develop a spectral domain analysis method and show that the same-frequency nonreciprocity is a result of the nonreciprocal frequency conversion to the intermodulation (IM) frequencies by the time-varying resonators. With appropriate modulation frequency, modulation depth, and phase delay, the signal power at the IM frequencies is converted back to the RF frequency and adds up constructively to form a low-loss forward passband, whereas they add up destructively in the reverse direction to create the isolation. To validate the theory, a lumped-element three-pole 0.04-dB ripple isolating filter with a center frequency of 200 MHz and a ripple bandwidth of 30 MHz is designed, simulated, and measured. When modulated with a sinusoidal frequency of 30 MHz, a modulation index of 0.25, and an incremental phase difference of 45°, the filter achieves a forward insertion loss of 1.5 dB and a reverse isolation of 20 dB. The measured nonmodulated and modulated results agree very well with the simulations. Such nonreciprocal filters may find applications in wideband simultaneous transmit and receive radio front ends.**

Manuscript received October 7, 2018; revised January 15, 2019; accepted March 4, 2019. Date of publication April 18, 2019; date of current version June 4, 2019. This work was supported in part by the Defense Advanced Research Projects Agency under Grant HR0011-17-C-0029, in part by the National Science Foundation with CAREER Grant No. ECCS-1749177, in part by a Mobility Grant from the Spanish Ministry of Education Ref. PRX18/00092, Projects TEC2016-75934-C4-4-R and 19494/PI/14, in part by a projects grant from the National Natural Science Foundations of China No. 61601234, and in part by a fellowship from the Postdoctoral International Exchange Program of China Postdoctoral Science Foundation (CPSF). *(Xiaohu Wu and Xiaoguang Liu are co-first authors.) (Corresponding author: Xiaohu Wu.)*

X. Wu is with the School of Electronic and Information Engineering, Nanjing University of Information Science and Technology, Nanjing 210044, China, and also with the Department of Electrical and Computer Engineering, University of California at Davis, Davis, CA 95616 USA (e-mail: xhwu@ieee.org).

X. Liu and J. S. Gómez-Díaz are with the Department of Electrical and Computer Engineering, University of California at Davis, Davis, CA 95616 USA (e-mail: lxgliu@ucdavis.edu; jsgomez@ucdavis.edu).

M. D. Hickle was with the School of Electrical and Computer Engineering, Purdue University, West Lafayette, IN 47907 USA. He is now with BAE Systems, Inc., Merrimack, NH 03054 USA (e-mail: mark.hickle@baesystems.com).

D. Peroulis is with the School of Electrical and Computer Engineering, Purdue University, West Lafayette, IN 47907 USA (e-mail: dperouli@purdue.edu).

A. Álvarez Melcón is with the Department of Information and Communication Technologies, Technical University of Cartagena, 30202 Murcia, Spain (e-mail: alejandro.alvarez@upct.es).

Color versions of one or more of the figures in this paper are available online at http://ieeexplore.ieee.org.

Digital Object Identifier 10.1109/TMTT.2019.2908868

***Index Terms*— Bandpass filter (BPF), isolator, nonreciprocity, spatiotemporal modulation (STM), time-invariant, time-modulated, time-varying.**

## I. Introduction

NONRECIPROCAL microwave components, such as circulators, isolators, and gyrators, are important building blocks in many wireless systems to prevent undesirable reflections [1]. They can also be used to allow transmitting and receiving simultaneously at the same frequency, thereby increasing the channel capacity without requiring more bandwidth [2]–[5]. In general, a linear time-invariant circuit consisting of materials with symmetric electric permittivity and magnetic permeability tensors is reciprocal. To achieve nonreciprocity, one of these conditions must be circumvented [6].

Traditionally, nonreciprocal components are constructed using magnetic materials, in which the internal magnetic moment of the material breaks the reciprocity when biased with a static magnetic field [7]–[11]. However, magnetic circulators and isolators are generally bulky and expensive. As an ever-increasing number of functionalities of a microwave system are now realized in integrated circuit (IC) form, circulators and isolators remain a bottleneck of integration.

To overcome the integration issue, nonreciprocity has been attempted by using active devices, such as transistors. Nonreciprocal circuits in the discrete form [12]–[14] or embedded within metamaterials [15] have been demonstrated. However, active device-based circulators/isolators generally suffer from poor noise figure and limited power handling, therefore yield a moderate/low dynamic range [16]. In addition, broadband power-dependent nonreciprocity has been demonstrated in [17], by combining the nonlinear Lorentzian and Fano resonators with a certain type of delay lines, an approach limited to a range of high-intensity signals exciting a single port at the time.

Recently, magnetless nonreciprocal devices based on time-varying circuits have received significant attention. The intensity-independent modulation provides great design flexibility, which has allowed researchers to put forward a wide variety of magnetless nonreciprocal devices in electromagnetics and acoustics [18]–[21]. In [21], a transmission line periodically loaded with time-varying capacitors is shown to exhibit nonreciprocity. The capacitors are modulated by a

sinusoidal signal with a progressive delay. Since the modulation is both time and location dependent, the modulation scheme is referred to as "spatiotemporal" modulation (STM). Nonreciprocity in [21] is observed from the RF carrier to the mixing products, and a frequency diplexer is used to separate the signals traveling in opposite directions. In the implementation, a relatively long loaded transmission line of $3.9\lambda_g$ and a modulation frequency higher than the RF frequency are needed, both of them present challenges in miniaturization and power consumption.

Nonreciprocity can also be realized by using the angular-momentum biasing in a ring or loop structure to mimic the Faraday effect in magnetic materials. In [22], circulating the fluid physically in a resonant ring cavity splits the ring's azimuthal resonant modes and produces significant acoustic nonreciprocity. In the electronic domain, STM has been used to achieve angular-momentum biasing and nonreciprocity [23]–[29]. For example, in [23], angular momentum-biased devices are presented in a ring structure with continuous capacitive loading. STM is introduced across the transverse surface area of the ring, leading to an effective electric rotation and strong nonreciprocity at the subwavelength scale. In [24], the composite loop of three discrete shunt resonators in a $\Delta$ topology is presented. The resonant frequencies of the three resonators are modulated in time with 120° phase difference between each other. Deep isolation can be generated with a small modulation index and a modulation frequency of 20%–30% of the RF carrier frequency. In [25], three series resonators are connected in a Y topology to simplify the bias circuit. Three film bulk acoustic resonators (FBARs) in [27] and MEMS resonators in [28] are used in the same fashion to achieve nonreciprocity with a very small modulation frequency. Differential circulators are presented in [28]–[30] to cancel the undesired intermodulation (IM) products, which helps to improve the insertion loss, impedance matching, bandwidth, and noise figure. Three identical BPFs are used to broaden the isolation bandwidth of such spatiotemporally modulated circulator in [31].

In [32], ultrawideband nonreciprocity is achieved by sequentially switching between the transmission and receiving paths. Specifically, six transmission lines of equal length and five single-pole-double-throw switches are used to construct the circuit. The switch timing is synchronized with the delay in the transmission lines. In [33]–[35], gyrators with $\pm\pi/2$ phase nonreciprocity are realized through staggered commutation inside the N-path filters. Based on the same principle, two double-pole double-throw switches with $\lambda/4$ delay lines are properly synchronized to have nonreciprocity not only in phase but also in magnitude [36]. Approaches based on commutated gyrators are compact in size and compatible with integrated circuit fabrication. However, they require switching frequency to be the same as the center frequency of the nonreciprocal devices, leading to challenges in power consumption and suppressing clock leakage.

In this paper, we report the design of novel nonreciprocal bandpass filters (BPFs) that allow a signal to travel in only one direction using the STM principle, realizing an isolator and a BPF integrated into one device. Fig. 1 captures the concept

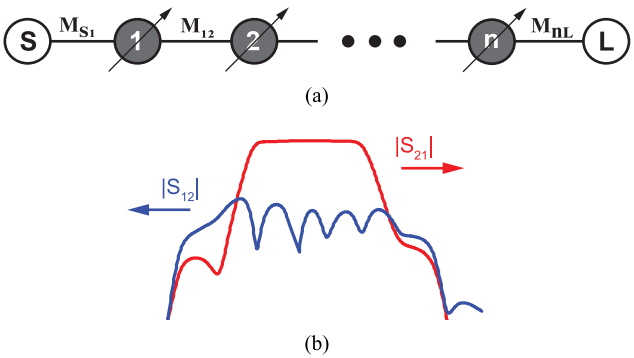


Fig. 1. (a) Topology diagram of the proposed time-modulated isolating filter. Black circles with arrow: time-modulated resonator with the angular frequency defined as $\omega_i = \omega_0\{1 + \xi\cos[\omega_m t + (i-1)\Delta\phi]\}$, $i = 1, 2, \ldots, N$; white circles: unitary source (S) and load (L); $M_{S1}$: coupling between source and resonator 1; $M_{nL}$: coupling between resonator $n$ and load. (b) Nonreciprocal forward transmission $|S_{21}|$ and backward transmission $|S_{12}|$, where port 1 refers to the source and port 2 refers to the load.

of this "isolating filter" that consists of a series of coupled resonators that are temporally modulated [37]. To understand the creation of nonreciprocity in such a structure, we utilize the spectral domain method to analyze the time-varying circuit. Essentially, each time-varying component in the circuit produces IM products. It can be shown that the energy conversion between the carrier and the IM frequencies is nonreciprocal, whereas energy transmission at the carrier frequency only is strictly reciprocal. We demonstrate that the same-frequency nonreciprocity at the carrier frequency can be achieved with low insertion loss in higher order modulated filters. We show that this is due to the additional degrees of freedom available with more time-varying elements to enable that nonreciprocal IM signals can be converted back to the transmission of the carrier frequency. As an experimental validation, a three-pole isolating filter is demonstrated to exhibit the flat in-band transmission, low insertion loss (1.5 dB), high reverse isolation (20 dB), and good matching (15 dB) at both ports. To the best of our knowledge, this is the first report of a two-port isolating circuit that exhibits strong same-frequency nonreciprocity.

This paper is organized as follows. Section II reviews the spectral domain analysis techniques for time-varying circuits and presents the full-spectral matrix theory for the most general form of spatiotemporal-modulated circuits. Section III presents the full-spectral matrix analysis for filters, including a single resonator, two-pole filter, and three-pole filter. The numerical convergence is also discussed. Section IV presents the design of a three-pole isolating filter and its simulation and measurement results. Finally, the conclusions are given in Section V.

## II. Analysis of Time-Varying Circuits

The analysis of linear time-varying (LTV) circuits with time-harmonic variations is well understood with the spectral domain method [38]. To set the background for further analysis, this section presents a review of such a method and, based on the newly defined multidimensional full-spectral matrix,

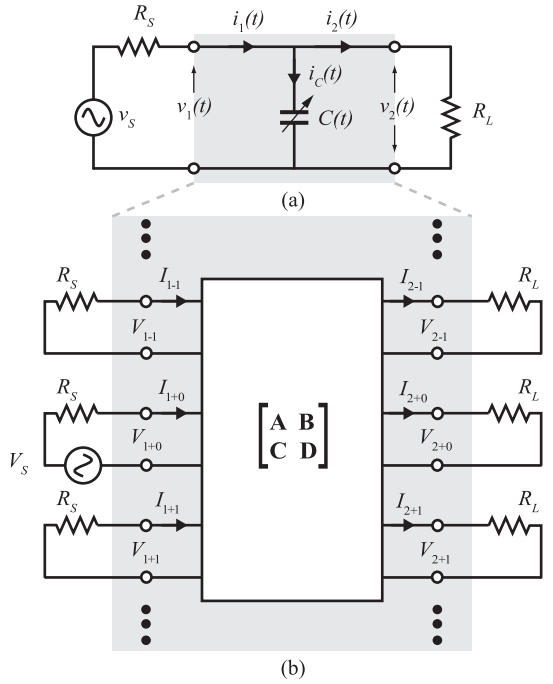


Fig. 2. (a) Simple LTV circuit with a single sinusoidally modulated shunt capacitor. (b) General spectral equivalent circuit with ports for all the IM frequencies.

the full spectral network parameter matrices are developed and expanded to consider devices composed of any number of time-modulated resonators, yielding to a rigorous spectral domain approach that is able to characterize the energy transmission and reflection in general time-varying networks.

Fig. 2 shows a basic LTV circuit with a single shunt time-varying capacitor $C(t)$. $V_S$ is the source with source impedance $R_S$ located at the left port (port 1) and a resistor terminal $R_L$ is located at the right port (port 2). $R_S$ and $R_L$ are time invariant and frequency independent. The variation of the capacitor is assumed to be time harmonic, that is

$$C(t) = C_0 + \Delta C \cos(\omega_m t + \phi) \tag{1}$$

where $C_0$ is the nominal (dc) capacitance, $\Delta C$ is the modulation depth, $\omega_m$ is the modulation angular frequency, and $\phi$ is the phase shift of the modulating waveform. A modulation index parameter $\xi$ is defined as

$$\xi = \frac{\Delta C}{C_0}. \tag{2}$$

The voltages and currents of the two-port network consisting of a shunt capacitor only are related by

$$v_1(t) = v_2(t) \tag{3a}$$

$$\int_0^t i_1(\tau)d\tau = C(t)v_2(t) + \int_0^t i_2(\tau)d\tau. \tag{3b}$$

Since the modulation is periodic, we can represent (3) in the frequency domain by its Fourier series. Note that the port voltages and currents should contain not only the RF carrier signal at $\omega$ but also all the IM products at $\omega \pm n\omega_m$ ($n = 0, 1, 2, \ldots$), which is due to the sinusoidal modulation of the capacitor [38]. The spectral frequency matrix $\boldsymbol{\omega}$ is defined to capture all the spectral frequencies in the time-varying circuits, where all the off-diagonal elements are zero

$$\boldsymbol{\omega} = \text{diag}(\ldots, \omega - 2\omega_m, \omega - \omega_m, \omega, \omega + \omega_m, \omega + 2\omega_m, \ldots). \tag{4}$$

Therefore, in the frequency domain, the port voltages and currents take the form of vectors, namely, $\boldsymbol{V_i} = [\ldots, V_{i-2}, V_{i-1}, V_{i+0}, V_{i+1}, V_{i+2}, \ldots]$ and $\boldsymbol{I_i} = [\ldots, I_{i-2}, I_{i-1}, I_{i+0}, I_{i+1}, I_{i+2}, \ldots]$. Here, $V_{i\pm n}$ and $I_{i\pm n}$ ($i = 1, 2$, $n = \mathbb{Z}$) are the phasor representation of the voltage and current of port $i$ at frequency $\omega \pm n\omega_m$, respectively.

The frequency domain form of (3) is then

$$\begin{bmatrix} \boldsymbol{V_1} \\ \boldsymbol{I_1} \end{bmatrix} = \begin{bmatrix} \mathbf{U} & \mathbf{0} \\ \mathbf{Y_C} & \mathbf{U} \end{bmatrix} \begin{bmatrix} \boldsymbol{V_2} \\ \boldsymbol{I_2} \end{bmatrix} \tag{5}$$

where $\mathbf{0}$ is the zero matrix, $\mathbf{U}$ is the unity matrix, and $\mathbf{Y_C}$ is the spectral admittance matrix of the shunt time-varying capacitor, as given in (6), shown at the bottom of the next page. It should be noted that (5) also reveals the spectral **ABCD** matrix of the temporally modulated capacitor. Theoretically, the dimensions of $\mathbf{0}$, $\mathbf{U}$, and $\mathbf{Y_C}$ are infinite because the modulation of the capacitor generates infinite number of IM products at frequencies $\omega \pm n\omega_m$. In practice, only a limited number of IM products need to be considered for a given accuracy requirement.

To make the notation more intuitive, we base the element indices of $\mathbf{Y_C}$ in the center of the matrix and use them to indicate the frequency, i.e., $Y_{C,(\pm n_1,\pm n_2)}$ represents the admittance/transconductance from frequency $\omega \pm n_1\omega_m$ to frequency $\omega \pm n_2\omega_m$. The diagonal elements $Y_{C,(\pm n_1,\pm n_1)}$ correspond to the admittance of the time-varying capacitor at each IM frequency. The off-diagonal elements $Y_{C,(\pm n_1,\pm n_2)}$ ($n_1 \neq n_2$) correspond to the transconductance from frequency $\omega \pm n_1\omega_m$ to frequency $\omega \pm n_2\omega_m$.

It is clear from (6) that $Y_{C,(n_1,n_2)}$ and $Y_{C,(n_2,n_1)}$ ($n_1 \neq n_2$) are not equal to each other. For example,

$$Y_{C,(-1,0)} = (\omega - \omega_m)\frac{\xi}{2}e^{-j\phi} \tag{7}$$

whereas

$$Y_{C,(0,-1)} = \omega\frac{\xi}{2}e^{j\phi}. \tag{8}$$

There is not only a difference in the magnitude but also a difference in the phase when $\phi \neq 0$. Although the simple circuit with only one time-varying element exhibits no nonreciprocity at the RF carrier frequency, this asymmetry in the transconductance between a pair of IM frequencies forms the basis of the nonreciprocal behavior achieved in our proposed isolating filter.

Equations (5) and (6) indicate that the RF carrier at $\omega$ is upconverted and downconverted to all the IM frequencies by the time-varying capacitor. As such, an equivalent circuit of the capacitor must contain ports for all the IM frequencies, as shown in Fig. 2(b). By exploring the network parameters in the defined full-spectral matrix space, a more comprehensive solution can be derived from (5) and the general equivalent circuit of Fig. 2(b) to illustrate the energy transmission and reflection among all the spectral frequencies.

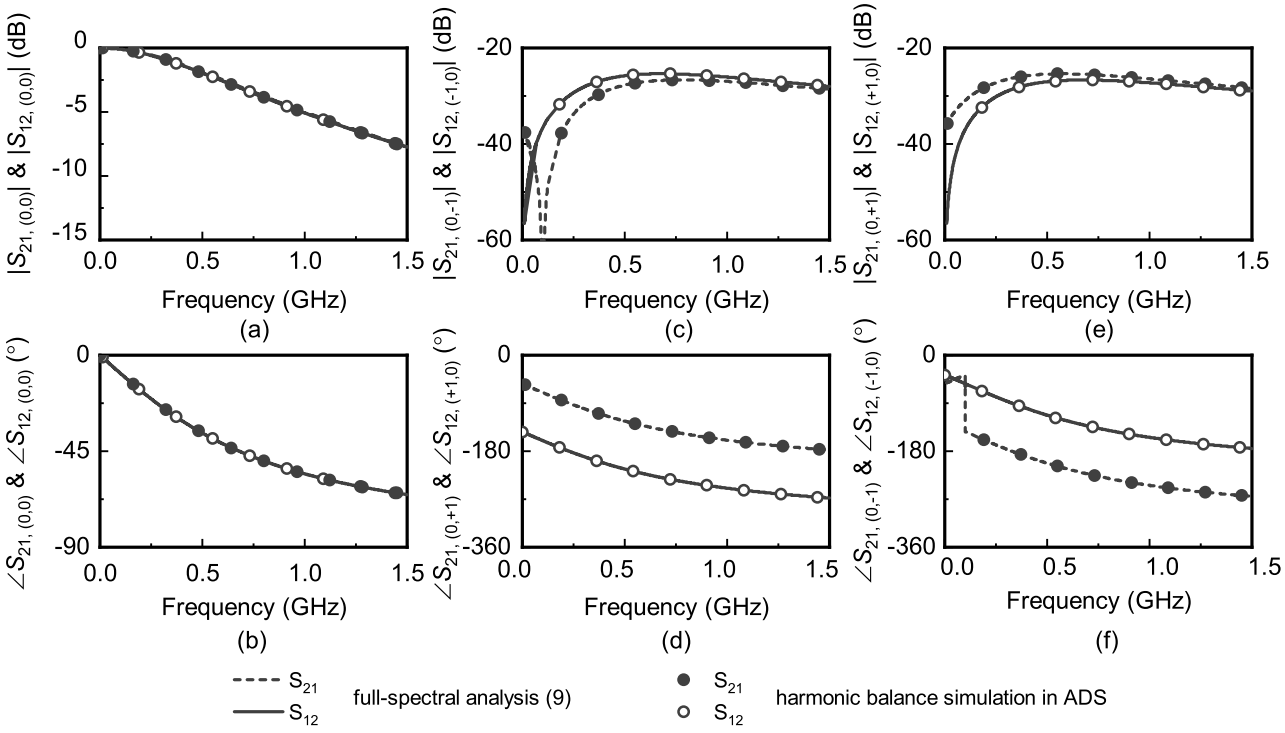


Fig. 3. Synthesized and simulated transmission properties of a single time-varying capacitor in Fig. 2. (a) $|S_{21,(0,0)}|$ and $|S_{12,(0,0)}|$. (b) $\angle S_{21,(0,-2)}$ and $\angle S_{12,(0,-2)}$. (c) $|S_{21,(0,+1)}|$ and $|S_{12,(+1,0)}|$. (d) $\angle S_{21,(0,+1)}$ and $\angle S_{12,(+1,0)}$. (e) $|S_{21,(0,-1)}|$ and $|S_{12,(-1,0)}|$. (f) $\angle S_{21,(0,-1)}$ and $\angle S_{12,(-1,0)}$.

The S-parameters of the two-port network representing the time-varying capacitor are shown in (9) at the bottom of this page. The detailed procedures of the derivation are given in the Appendix. Note that each $\mathbf{S_{ij}}$ is a matrix of similar dimensions as $\mathbf{Y_C}$ to represent the interactions between different IM frequencies.

To validate the presented full-spectral analysis, we present, in Fig. 3, the simulated and calculated S-parameters of the circuit in Fig. 2(a). Here, the source and load impedances are both set to be 50 Ω. The time-varying capacitance has a nominal value of 9.6 pF, a modulation index of $\xi = 0.2$, a modulation frequency of $f_m = 100$ MHz, and a starting phase of $\phi_0 = 45°$.

Fig. 3(a) and (b) shows the transmission between the RF carrier frequency $\omega$ at port 1 and $\omega$ at port 2, denoted by $S_{21,(0,0)}$ and $S_{12,(0,0)}$. Here, we follow the same index notation

$$\begin{array}{c} \cdots \quad -\mathbf{2} \quad\quad -\mathbf{1} \quad\quad \mathbf{0} \quad\quad +\mathbf{1} \quad\quad +\mathbf{2} \quad\quad \cdots \ \textbf{indices} \\ \mathbf{Y_C} = jC_0 \begin{bmatrix} \ddots & \vdots & \vdots & \vdots & \vdots & \vdots & \iddots \\ \cdots & (\omega-2\omega_m) & (\omega-2\omega_m)\frac{\xi}{2}e^{-j\phi} & 0 & 0 & 0 & \cdots \\ \cdots & (\omega-\omega_m)\frac{\xi}{2}e^{j\phi} & (\omega-\omega_m) & (\omega-\omega_m)\frac{\xi}{2}e^{-j\phi} & 0 & 0 & \cdots \\ \cdots & 0 & \omega\frac{\xi}{2}e^{j\phi} & \omega & \omega\frac{\xi}{2}e^{-j\phi} & 0 & \cdots \\ \cdots & 0 & 0 & (\omega+\omega_m)\frac{\xi}{2}e^{j\phi} & (\omega+\omega_m) & (\omega+\omega_m)\frac{\xi}{2}e^{-j\phi} & \cdots \\ \cdots & 0 & 0 & 0 & (\omega+2\omega_m)\frac{\xi}{2}e^{j\phi} & (\omega+2\omega_m) & \cdots \\ \iddots & \vdots & \vdots & \vdots & \vdots & \vdots & \ddots \end{bmatrix} \begin{array}{c} \vdots \\ -\mathbf{2} \\ -\mathbf{1} \\ \mathbf{0} \\ +\mathbf{1} \\ +\mathbf{2} \\ \vdots \end{array} \end{array} \tag{6}$$

$$\begin{bmatrix} \mathbf{S_{11}} & \mathbf{S_{12}} \\ \mathbf{S_{21}} & \mathbf{S_{22}} \end{bmatrix} = \begin{bmatrix} \mathbf{U} - 2[\mathbf{U} + (\mathbf{A}R_2 + \mathbf{B})(\mathbf{C}R_1R_2 + \mathbf{D}R_1)^{-1}]^{-1} & 2[\mathbf{U} + (\mathbf{A}R_2 + \mathbf{B})(\mathbf{C}R_2 + \mathbf{D})^{-1}/R_1]^{-1} \\ & \times[\mathbf{A} - (\mathbf{A}R_2 + \mathbf{B})(\mathbf{C}R_2 + \mathbf{D})^{-1}\mathbf{C}] \\ 2\sqrt{\frac{R_S}{R_L}}[\mathbf{A} + \mathbf{B}/R_2 + \mathbf{C}R_1 + \mathbf{D}R_1/R_2]^{-1} & \mathbf{U} - 2[\mathbf{U} + (\mathbf{A}R_2 + \mathbf{C}R_1R_2)^{-1}(\mathbf{B} + \mathbf{D}R_1)]^{-1} \end{bmatrix} \tag{9}$$

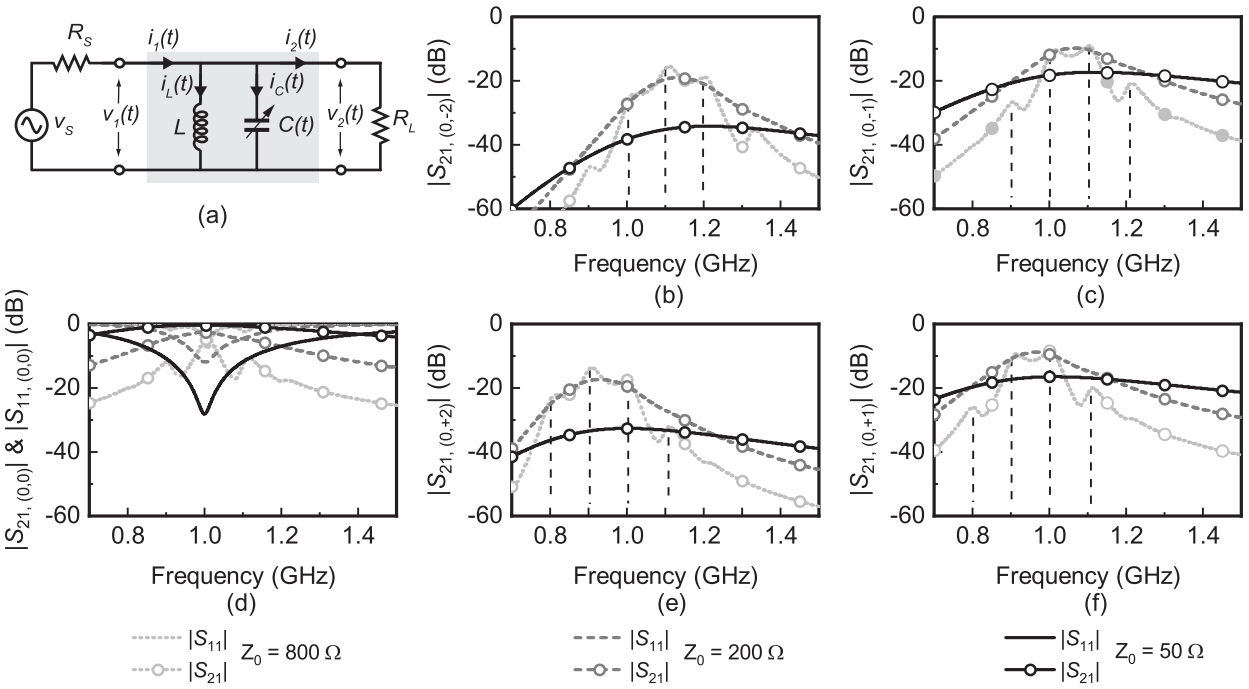


Fig. 4. (a) Shunt $LC$ resonator with time-invariant inductor $L$ and time-varying capacitor $C(t)$. (b) $|S_{21,(0,-2)}|$. (c) $|S_{21,(0,-1)}|$. (d) $|S_{21,(0,0)}|$. (e) $|S_{21,(0,+2)}|$. (f) $|S_{21,(0,+1)}|$.

of $\mathbf{Y_C}$ as in (6) for the S-parameters. As expected, the circuit is reciprocal at $\omega$. The full-spectral solution of (9) agrees exactly with the harmonic balance simulation in the Keysight Advanced Design System (ADS). Fig. 3(c) and (d) shows the transmission between $\omega$ and $\omega - \omega_m$ ($S_{21,(0,-1)}$ and $S_{12,(0,-1)}$). A nonreciprocal behavior is clearly observed in both magnitude and phase. Note that the phase difference between $S_{21,(0,-1)}$ and $S_{12,(0,-1)}$ is exactly 90° ($2\phi$). Similar behaviors are observed for the transmission between $\omega$ and $\omega+\omega_m$, as shown in Fig. 3(e) and (f). Consequently, the full-spectral method of (9) will be used throughout this paper to analyze the time-varying circuits.

## III. Time-Varying Resonators and Filters

### A. Time-Modulated Resonator

The analysis presented in Section II can be extended to time-varying resonators that form the building blocks of many STM circuits [25]. Fig. 4(a) shows a simple shunt time-varying $LC$ resonator consisting of a time-invariant inductor $L$ and a time-varying capacitor $C(t)$. The spectral admittance of the shunt time-varying $LC$ resonator is simply $\mathbf{Y_{LC}} = \mathbf{Y_L} + \mathbf{Y_C}$, where $\mathbf{Y_L} = (j\boldsymbol{\omega}L)^{-1}$ is the spectral admittance of $L$. Here, $\boldsymbol{\omega}$ is the diagonal frequency matrix given by (4). Thus, the spectral **ABCD** matrix of the time-varying resonator is

$$\mathbf{N_{LC}} = \begin{bmatrix} \mathbf{U} & \mathbf{0} \\ \mathbf{Y_{LC}} & \mathbf{U} \end{bmatrix}. \tag{10}$$

The performance of the circuit may be solved in a similar fashion, as shown in (9). Fig. 4(b)–(f) shows the simulated transmission from $\omega$ to $\omega - 2\omega_m$ ($S_{21,(0,-2)}$), from $\omega$ to $\omega - \omega_m$ ($S_{21,(0,-1)}$), from $\omega$ to $\omega$ ($S_{21,(0,0)}$), from $\omega$ to $\omega + 2\omega_m$ ($S_{21,(0,+2)}$), and from $\omega$ to $\omega + \omega_m$ ($S_{21,(0,+1)}$), respectively. The power reflection from $\omega$ to $\omega$ ($S_{11,(0,0)}$ is also inserted in Fig. 4(d). Since the power reflected from $\omega$ to $\omega \pm n\omega_m$ ($S_{11,(0,\pm n)}$) is exactly the same as the power transmitted from $\omega$ to $\omega \pm n\omega_m$ ($S_{21,(0,\pm n)}$) for a single shunt time-varying resonator, and thus, $S_{11,(0,\pm n)}$ is not shown in Fig. 4(b), (c), (e), and (f). Here, the time-varying capacitance has a nominal value of 9.6 pF, which resonates with a static inductor of 2.6 nH at 1 GHz. Modulation is applied to the capacitor with $f_m = 100$ MHz, $\xi = 0.2$, and $\phi_0 = 45°$.

A few observations can be made. First, the transmission is a strong function of the port impedances ($R_S = R_L$) seen by the resonator. Around the static center frequency of 1 GHz, the transmission at $\omega$ decreases, whereas the transmission from $\omega$ to the IM frequencies increases, as $R_S$ ($R_L$) increases. A qualitative explanation for this is that $C(t)$ is effectively shorted by $R_S$ ($R_L$) when $R_S$ ($R_L$) is small compared to $1/j\omega C(t)$. As a result, the effect of the modulation is small, and most of the available source power is delivered to the load.

When $R_S$ ($R_L$) is larger, the effect of the capacitance modulation is stronger. More power is converted to the IM frequencies, and as a result, the transmission at $\omega$ becomes weaker. As $R_S$ ($R_L$) increases, the effective loaded quality factor $Q_L$ at $\omega$ and the IM frequencies increases, as is the case for static resonators. The higher $Q_L$ allows us to observe the frequency translation characteristics of the circuit; distinctive peaks at IM frequencies can be observed in the transmission between frequencies.

When the time-varying resonator is used in a more complicated circuit, such as the STM circulator [25] and filter presented later in this paper, the impedances presented to the resonator may vary over a large range depending on

the strength of the couplings between the resonators. As a result, a significant portion of the power may be converted to and back from the IM frequencies to create nonreciprocal transmission characteristics.

### B. Filters—Introducing Spatial Modulation

From the above-mentioned analysis, we have seen that for time-varying circuits containing only one time-varying component, nonreciprocity cannot be observed at the RF carrier frequency although the conversion between different frequencies is nonreciprocal. To achieve the same-frequency nonreciprocity, more than one time-varying component is needed. The rationale is illustrated qualitatively in Fig. 4.

With one time-varying component, the available power from the carrier frequency is spread among the carrier frequency and all the IM frequencies. The power that is transmitted and reflected to the IM frequencies shows up as a loss when we consider the transmission at the carrier frequency ($S_{21,(0,0)}$). When more time-varying components are added to the system, the transmitted and reflected IM products may be upconverted and downconverted back to the carrier frequency. Because $S_{21,(0,0)}$ now contains contributions from frequency translation, and that frequency translation is nonreciprocal, $S_{21,(0,0)}$ may become nonreciprocal as well. More importantly, under the right modulation parameters, the power at the IM frequencies may be collected back at the carrier frequency constructively, and a low insertion loss may be achieved.

To demonstrate this, we first study the behavior of a two-pole filter composed of dual time-varying resonators. Fig. 5 shows the circuit topology of the two-pole filter. Here, ideal admittance inverters are used to realize the interresonator and external couplings. The two resonators are modulated by modulating the capacitors as follows:

$$C_i(t) = C_{0i}[1 + \xi_i \cos(\omega_{mi} t + \phi_i)], \quad i = 1,\ 2. \tag{11}$$

In general, the modulation conditions for the two resonators are different not only in time but also in space, hence the notion "STM" in isolating filters.

The response of the filter can be analyzed following the same framework presented in Section II. Take the filter in Fig. 5(a) for example, the spectral **ABCD** of the filter is a cascade of the **ABCD** that describes the inverters and the resonators, that is

$$\mathbf{N_2} = \mathbf{N_{J_{S1}}} \mathbf{N_{LC_1}} \mathbf{N_{J_{12}}} \mathbf{N_{LC_2}} \mathbf{N_{J_{2L}}} \tag{12}$$

where $\mathbf{N_{J_{S1}}}$, $\mathbf{N_{J_{12}}}$, and $\mathbf{N_{J_{2L}}}$ are the spectral **ABCD** matrices of the J-inverters and $\mathbf{N_{LC_1}}$ and $\mathbf{N_{LC_2}}$ are the spectral **ABCD** matrices of the first and second shunt $LC$ resonators, respectively.

To derive the spectral **ABCD** matrix of the inverters in a multispectral network [see Fig. 2(b)], we consider the voltage–current relationship of admittance inverters [1]

$$V_{1\pm n} = \pm \frac{1}{jJ} I_{2\pm n} \tag{13a}$$

$$I_{1\pm n} = \mp jJ V_{2\pm n} \tag{13b}$$

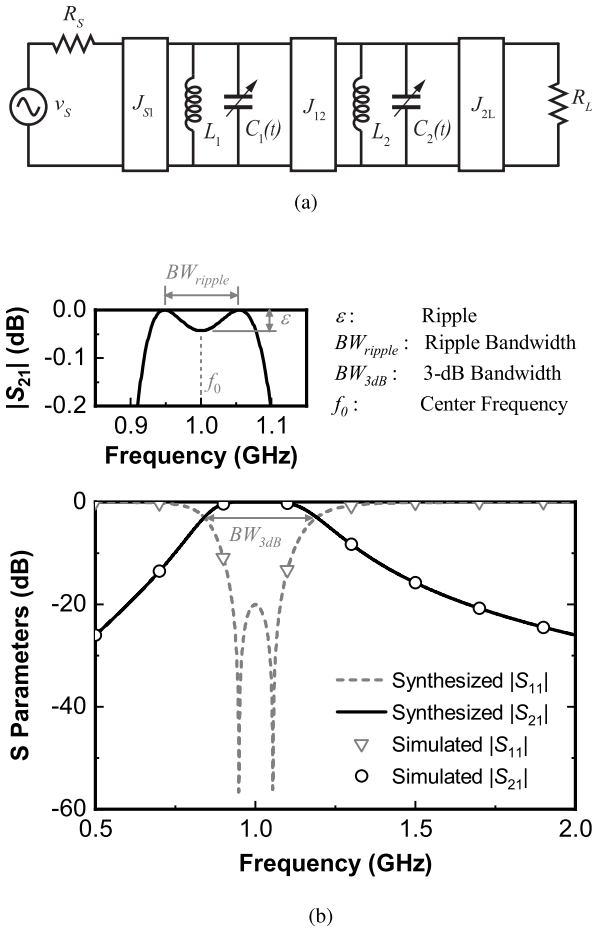


Fig. 5. (a) Topology of the second-order spatiotemporally modulated filter. (b) Simulated responses of nonmodulated two-pole BPF ($J_{S1} = J_{2L} = 0.0134\ \Omega^{-1}$, $J_{12} = 0.01\ \Omega^{-1}$, $R_S = R_L = 50\ \Omega$, $L_1 = 4$ nH, $L_2 = 4$ nH, $C_{01} = 6.37$ pF, and $C_{02} = 6.37$ pF).

where $n$ refers to the excitation modes into inverters and is defined in the definition of the port voltage and current vectors ($\boldsymbol{V_i}$ and $\boldsymbol{I_i}$) in Section II.

Therefore, the spectral **ABCD** matrix of the time-invariant J-inverters can be given as

$$\mathbf{N_J} = \begin{bmatrix} \mathbf{0} & \pm\frac{1}{jJ}\mathbf{U} \\ \mp jJ\mathbf{U} & \mathbf{0} \end{bmatrix}. \tag{14}$$

When considering only the carrier frequency, i.e., a time-invariant network, (14) reduces to

$$N_J = \begin{bmatrix} 0 & \pm\frac{1}{jJ} \\ \mp jJ & 0 \end{bmatrix}$$

which is the conventional ABCD matrix of J-inverters [1].

Substituting (10) and (14) into (12) gives

$$\mathbf{N_2} = \begin{bmatrix} \frac{J_{2L}\mathbf{Y_{LC_1}}}{jJ_{S1}J_{12}} & \frac{\mathbf{Y_{LC_1}}\mathbf{Y_{LC_2}} + J_{12}^2\mathbf{U}}{jJ_{S1}J_{12}J_{2L}} \\ \frac{J_{S1}J_{2L}\mathbf{U}}{jJ_{12}} & \frac{J_{S1}\mathbf{Y_{LC_2}}}{jJ_{12}J_{2L}} \end{bmatrix}. \tag{15}$$

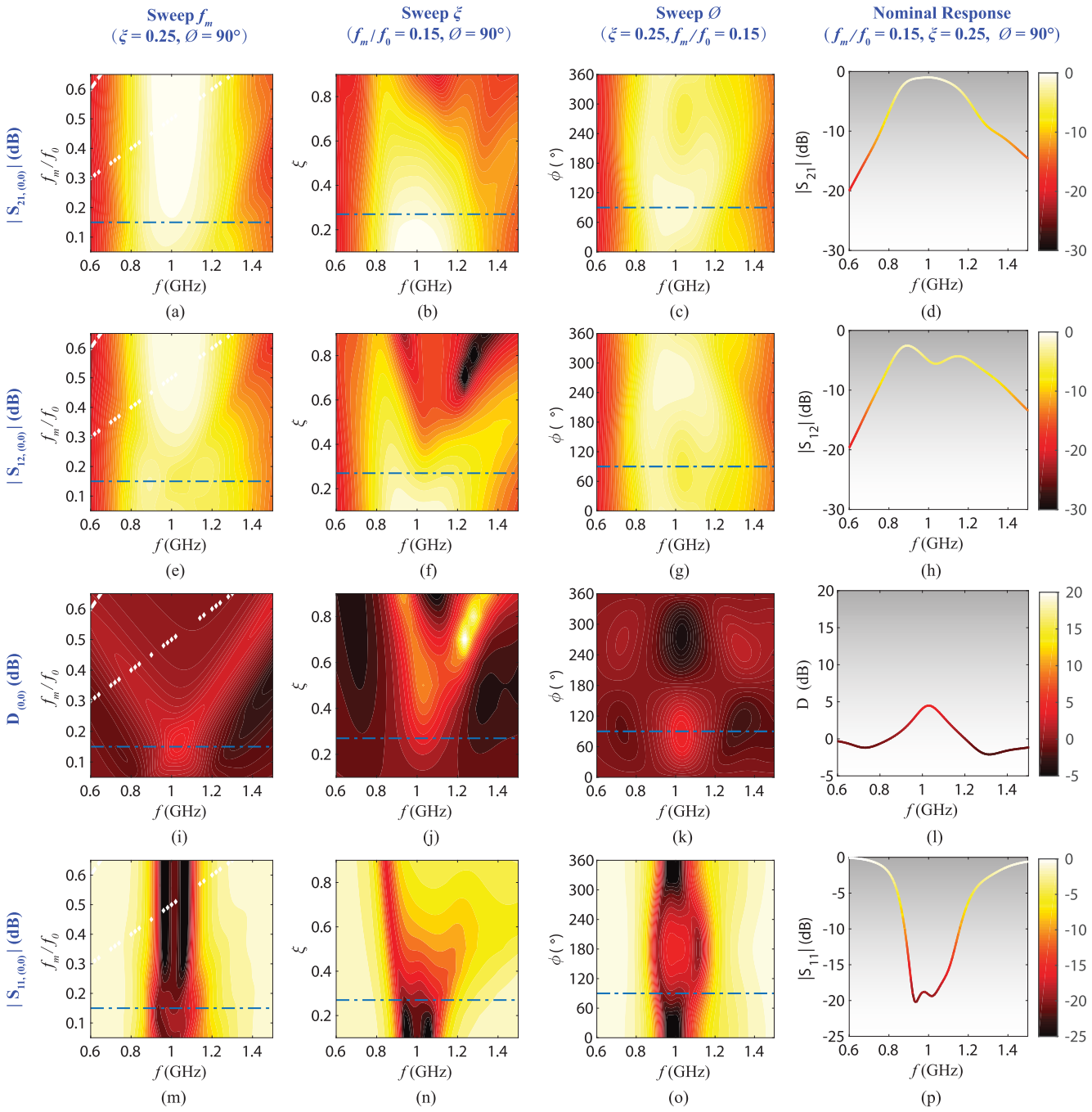


Fig. 6. Parametric studies of second-order filter (the blue dashed–dotted line is to mark the nominal responses in the parametric studies). (a) Modulated $|S_{21,(0,0)}|$ with varied $f_m$. (b) Modulated $|S_{21,(0,0)}|$ with varied $\xi$. (c) Modulated $|S_{21,(0,0)}|$ with varied $\phi$. (d) Synthesized $|S_{21,(0,0)}|$ with $f_m = 0.15 f_0$, $\xi = 0.25$, and $\phi = 90°$. (e) Modulated $|S_{12,(0,0)}|$ with varied $f_m$. (f) Modulated $|S_{12,(0,0)}|$ with varied $\xi$. (g) Modulated $|S_{12,(0,0)}|$ with varied $\phi$. (h) Synthesized $|S_{12,(0,0)}|$ with $f_m = 0.15 f_0$, $\xi = 0.25$, and $\phi = 90°$. (i) Modulated $D_{(0,0)}$ with varied $f_m$. (j) Modulated $D_{(0,0)}$ with varied $\xi$. (k) Modulated $D_{(0,0)}$ with varied $\phi$. (l) Synthesized $D_{(0,0)}$ with $f_m = 0.15 f_0$, $\xi = 0.25$, and $\phi = 90°$. (m) Modulated $|S_{11,(0,0)}|$ with varied $f_m$. (n) Modulated $|S_{11,(0,0)}|$ with varied $\xi$. (o) Modulated $|S_{11,(0,0)}|$ with varied $\phi$. (p) Synthesized $|S_{11,(0,0)}|$ with $f_m = 0.15 f_0$, $\xi = 0.25$, and $\phi = 90°$.

To give a numerical design example, we start with a static two-pole filter with a 0.043-dB Chebyshev response, 150-MHz equal-ripple bandwidth (3-dB bandwidth of 350 MHz), and a normalized center frequency of 1 GHz [see Fig. 5(b)]. In the time-varying case, for simplicity, the two resonators are modulated with the same modulation index and modulation frequency but with different modulation phase. Since only the phase difference is of significance here, $\phi_1$ is set to 0 and $\phi_2$ is set to be $\Delta\phi$.

It is observed from Fig. 5(b) that when $\xi = 0$, i.e., there is no modulation, the calculated filter response from (15) agrees exactly with the simulated static response. Next, the frequency response of the two-pole filter is studied by changing the modulation parameters $f_m$, $\xi$, and $\Delta\phi$. The results of the study are shown in Fig. 6. The first three columns of Fig. 6 show the calculated filter frequency response with respect to $f_m$, $\xi$, and $\phi$, respectively. The fourth column shows the calculated filter frequency responses for the nominal values

of $f_m = 0.15\ f_0$, $\xi = 0.15$, and $\Delta\phi = 90°$. The four rows of Fig. 6 show $|S_{21,(0,0)}|$, $|S_{12,(0,0)}|$, $D_{(0,0)}$, and $|S_{11,(0,0)}|$, respectively. Here, $D_{(0,0)}$ is defined as $D_{(0,0)} = S_{21}$ (dB) $-$ $S_{12}$ (dB) to quantify the level of magnitude nonreciprocity at the carrier frequency, which implies the directivity of the isolating filters.

The modulated filter exhibits the same-frequency nonreciprocity under most combinations of $f_m$, $\xi$, and $\Delta\phi$. With respect to $f_m$ (first column of Fig. 6), it is observed that the modulated filter exhibits the strongest $D_{(0,0)}$ (approximately 5 dB at 1 GHz) when $f_m$ is approximately the same as the equiripple bandwidth (150 MHz) of the filter. At this $f_m$, $S_{21,(0,0)}$ maintains the filter shape reasonably well with a minimum insertion loss of 0.6 dB. Increasing $f_m$ improves the insertion loss at the cost of $D_{(0,0)}$.

With respect to the modulation index $\xi$, it is observed that a smaller $\xi$ results in better insertion loss. This is expected, as the filter approaches the static design as $\xi$ decreases to 0. Although $D_{(0,0)}$ reaches a very high value of approximately 20 dB for $\xi > 0.6$, the corresponding insertion loss degrades too much to make it a practical design. As shown in Fig. 6(b), $\xi$ should be kept roughly less than 0.3 to maintain decent insertion loss. A conceptual explanation for this value relates the modulation to the filter's bandwidth. At a capacitance modulation depth of 0.3, the "instantaneous" resonant frequency of a modulated resonator is $\sqrt{1.3} \sim 1.15$ times of its static resonate frequency. At a center frequency of 1 GHz, in this example, this instantaneous frequency deviation is approximately a full bandwidth. As such, significant attenuation is presented to the carrier signal, causing a large degradation in the insertion loss. Thus, $\xi$ should be kept relatively small, e.g., around 0.25, to maintain the filter frequency response with low loss.

Not surprisingly, $S_{21,(0,0)}$ and $S_{12,(0,0)}$ are odd symmetric with respect to each other around the $\phi = 180°$ line. As a result, $D_{(0,0)}$ also exhibits odd symmetry with respect to $\phi = 180°$. When the two resonators are modulated in-phase ($\phi = 0$ or $360°$) or out-of-phase ($\phi = 180°$), $D_{(0,0)}$ is 0 dB, i.e., the modulated filter is reciprocal at the carrier frequency. However, the modulation translates a part of the carrier power to the IM frequencies, resulting in a high insertion loss of approximately 5 dB. Maximum $D_{(0,0)}$ and low insertion loss are achieved when $\phi$ is around $90°$.

At the nominal values of the modulation parameters, a good compromise between the insertion loss, return loss, and nonreciprocity is achieved (the fourth column of Fig. 6). Nevertheless, it is evident that a two-pole filter cannot achieve both high $D_{(0,0)}$ and good RF performance. We postulate that a better response can be achieved by adding more time-varying components so that more degrees of freedom can be utilized to convert the power at the IM frequencies back to the transmission of the carrier frequency.

### C. Isolating Three-Pole Bandpass Filter

In this section, we extend the study to a three-pole filter. We demonstrate that forward transmission $S_{21,(0,0)}$, reflection $S_{11,(0,0)}$, and reverse isolation $S_{12,(0,0)}$ can be achieved simultaneously with high directivity $D_{(0,0)}$.

Fig. 7(a) shows the circuit topology of the three-pole STM filter. The three resonators are modulated through time-varying capacitors, which are defined the same as in (11) with $i = 1, 2, 3$ corresponding to the three resonators, respectively. The spectral **ABCD** matrix of the filter $\mathbf{N_3}$ can be derived following the same framework as for (12), and it is shown in (16) at the bottom of this page. It should be noted that the same analysis can also be carried out for the $n$th-order filter network.

In this example, the three-pole filter is designed for the same static specifications as the two-pole filter presented in Section III-B, namely, a normalized center frequency of 1 GHz, a ripple level of 0.043 dB, and an equiripple bandwidth of 150 MHz (3-dB bandwidth of 231 MHz).

Parametric studies on the modulation parameters $f_m$, $\xi$, and $\phi$ are carried out, and the results are shown in Fig. 7. The general behavior of the three-pole STM filter follows those of the two-pole filter. However, a few distinguishing features in the three-pole STM filter are worth a discussion.

As shown in the first column of Fig. 7, when $f_m$ is larger than $0.3\,f_0$, both $|S_{21,(0,0)}|$ and $|S_{12,(0,0)}|$ are close to 0 dB, and the return loss is better than 20 dB with three deep reflection zeros across the passband. The filter is reciprocal at the RF center frequency. A similar behavior is actually observed in the two-pole filter, but it is more evident here. A conceptual explanation for this observation is that for large $f_m$, the IM frequencies ($\omega \pm n\omega_m$) fall outside of the filter bandwidth, and the signal power translated to these frequencies is very small. As such, $S_{21,(0,0)}$ contains a very little contribution from the frequency-translated components, and little nonreciprocity is observed.

When $f_m$ is smaller than $0.25\,f_0$, we start observing transmission zeros outside of the passband. These transmission zeros help improve the out-of-band rejection in the forward transmission characteristic of the filter. At the same time, the reflection zero number in the return loss reduces from 3 to 2 and eventually to 1, with a corresponding decrease

$$\begin{aligned}\mathbf{N_3} &= \mathbf{N_{J_{S1}}}\mathbf{N_{LC_1}}\mathbf{N_{J_{12}}}\mathbf{N_{LC_2}}\mathbf{N_{J_{23}}}\mathbf{N_{LC_3}}\mathbf{N_{J_{3L}}} \\ &= \begin{bmatrix} \dfrac{J_{3L}J_{12}^2\mathbf{U} + J_{3L}\mathbf{Y_{LC1}}\mathbf{Y_{LC2}}}{J_{S1}J_{12}J_{23}} & \dfrac{J_{23}^2\mathbf{Y_{LC1}} + J_{12}^2\mathbf{Y_{LC3}} + \mathbf{Y_{LC1}}\mathbf{Y_{LC2}}\mathbf{Y_{LC3}}}{J_{S1}J_{12}J_{23}J_{3L}} \\ \dfrac{J_{S1}J_{3L}\mathbf{Y_{LC2}}}{J_{12}J_{23}} & \dfrac{J_{S1}J_{23}^2\mathbf{U} + J_{S1}\mathbf{Y_{LC2}}\mathbf{Y_{LC3}}}{J_{12}J_{23}J_{3L}} \end{bmatrix}\end{aligned} \tag{16}$$

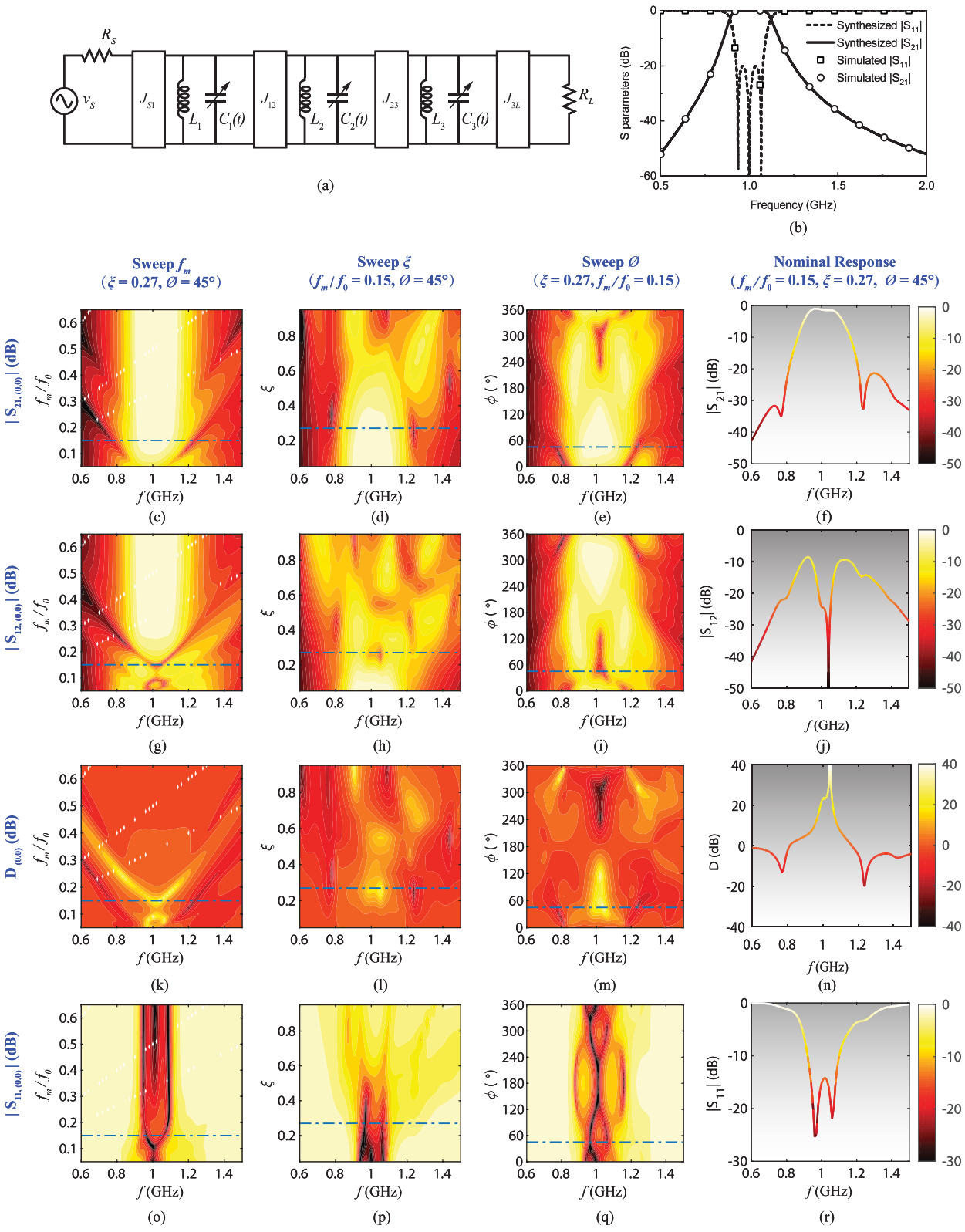


Fig. 7. Parametric studies of the three-pole filter ($J_{S1} = J_{3L} = 0.0119\ \Omega^{-1}$, $J_{12} = J_{23} = 0.0062\ \Omega^{-1}$, $R_S = R_L = 50\ \Omega$, $L_0 = 4$ nH, and static capacitor value $C_0 = 6.37$ pF). (a) Circuit topology of the three-pole filter. (b) Circuit responses without modulation. (c) Modulated $|S_{21,(0,0)}|$ with varied $f_m$. (d) Modulated $|S_{21,(0,0)}|$ with varied $\xi$. (e) Modulated $|S_{21,(0,0)}|$ with varied $\phi$. (f) Synthesized $|S_{21,(0,0)}|$ with $f_m = 0.15 f_0$, $\xi = 0.27$, and $\phi = 45°$. (g) Modulated $|S_{12,(0,0)}|$ with varied $f_m$. (h) Modulated $|S_{12,(0,0)}|$ with varied $\xi$. (i) Modulated $|S_{12,(0,0)}|$ with varied $\phi$. (j) Synthesized $|S_{12,(0,0)}|$ with $f_m = 0.15 f_0$, $\xi = 0.27$, and $\phi = 45°$. (k) Modulated $D_{(0,0)}$ with varied $f_m$. (l) Modulated $D_{(0,0)}$ with varied $\xi$. (m) Modulated $D_{(0,0)}$ with varied $\phi$. (n) Synthesized $D_{(0,0)}$ with $f_m = 0.15 f_0$, $\xi = 0.27$, and $\phi = 45°$. (o) Modulated $|S_{11,(0,0)}|$ with varied $f_m$. (p) Modulated $|S_{11,(0,0)}|$ with varied $\xi$. (q) Modulated $|S_{11,(0,0)}|$ with varied $\phi$. (r) Synthesized $|S_{11,(0,0)}|$ with $f_m = 0.15 f_0$, $\xi = 0.27$, and $\phi = 45°$.

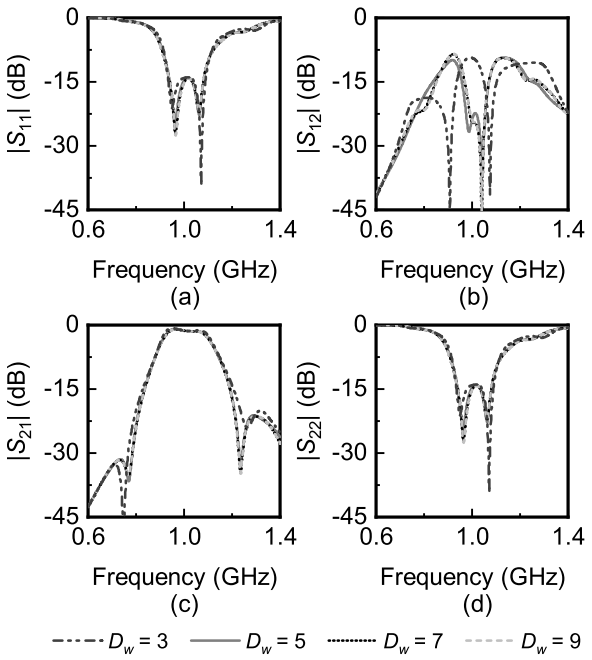


Fig. 8. Numerical results with increased dimensions of the spectral matrix $\boldsymbol{\omega}$: (a) $|S_{21}|$. (b) $|S_{12}|$. (c) $|S_{11}|$. (d) $|S_{22}|$. $D_{\boldsymbol{\omega}}$ is defined as the dimensions of the spectral frequency matrix. $\omega \pm \omega_m$ and $\omega$ are contained for $D_{\boldsymbol{\omega}} = 3$; $\omega \pm 2\omega_m$, $\omega \pm \omega_m$, and $\omega$ are contained for $D_{\boldsymbol{\omega}} = 5$; $\omega \pm 3\omega_m$, $\omega \pm 2\omega_m$, $\omega \pm \omega_m$, and $\omega$ are contained for $D_{\boldsymbol{\omega}} = 7$; $\omega \pm 4\omega_m$, $\omega \pm 3\omega_m$, $\omega \pm 2\omega_m$, $\omega \pm \omega_m$, and $\omega$ are contained for $D_{\boldsymbol{\omega}} = 9$.

in the return-loss bandwidth. A good compromise is reached at $f_m = 0.15 f_0$.

Similar to the two-pole case, a large modulation index $\xi$ causes significant degradation in the insertion loss. A moderate value of $\xi = 0.27$ results in low insertion loss and good reverse isolation across the equal-ripple bandwidth.

The three-pole STM filter also exhibits similar behavior as in the two-pole case with respect to $\Delta\phi$. An odd symmetric $D_{(0,0)}$ profile is observed with respect to $\Delta\phi = 180°$. Compared to the two-pole case, a much stronger $D_{(0,0)}$ can be observed for $\Delta\phi$ in the range of 30°–120°. A nominal value of $\Delta\phi = 45°$ is chosen for a widest bandwidth over which $D_{(0,0)}$ is maximized.

After the above-mentioned numerical studies, to have maximum isolation and good filter performance, the modulation parameters $f_m$, $\xi$, and $\phi$ are $0.15 f_0$, 0.27, and 45°, respectively.

The plots in the fourth column of Fig. 7 show the three-pole STM filter responses. The filter has a center frequency of 1 GHz, a minimum insertion loss of 1 dB, and a 3-dB bandwidth of 205 MHz. The reverse isolation is better than 25 dB. The return loss across the passband is better than 15 dB.

### *D. Numerical Convergence*

Theoretically, the IM products in a time-varying network are infinite and, therefore, would lead to an infinite dimensional full-spectral matrix. However, since the signal power is contained within low-order spectral frequencies, the matrix can be truncated to increase numerical efficiency while keeping high accuracy. Taking three-pole filter for an example, Fig. 8 shows the numerical results with a varied number of spectral frequencies. As the dimensions of the spectral matrix increased from 3 to 7, the numerical power transmission and reflection curves differ much, implying unconverged results. When the spectral matrix dimension increases to 7, the results tend to be stable and converged. The numerical studies also reveal that for a three-pole time-varying circuit, most of the signal power is constrained within $\omega \pm 3\omega_m$ since the transmission and reflection curves become stable with the spectral matrix dimension increased to be 7. The spectral matrix dimensions are truncated to be 3 and 5 for the single time-varying capacitor in Section II and two-pole filter in Section III-B, respectively. An extended conclusion can be deduced that for $n$-pole time-varying filtering network, the spectral matrix can be reduced to be $(2n + 1) \times (2n + 1)$ without losing numerical accuracy, where $n$ is the variable defined in the voltage and current vectors in Section II.

In summary, more than 1 time-varying circuit component is needed to achieve nonreciprocity on the RF carrier frequency. A minimal example of a two-pole filter with two capacitors modulated with a difference in phase demonstrates the existence of nonreciprocity. However, to achieve practical RF performances in terms of insertion loss, return loss, and isolation, higher order filters are needed to create sufficient degrees of freedom for the frequency-translated signals to be converted back to the carrier frequency. An example three-pole isolating filter shows that much better RF performance can be achieved when compared to the two-pole filter.

A general design procedure for the proposed isolating BPFs starts with the design of a proper static filter response. For optimum performance, the modulation frequency $f_m$ is chosen to be approximately equal to the filter's equal-ripple bandwidth $\mathrm{BW}_r$. The phase difference between the resonators $\Delta\phi$ should be chosen in the range of 30°–120°. Due to the complexity of the circuits, a numerical optimization or parameter study is inevitable to reach a good balance of the insertion loss, return loss, and isolation.

## IV. Experimental Validation

To validate the theory and the design strategy of isolating filters, a three-pole isolating filter is experimentally demonstrated in this section. The filter is designed for a 0.043-dB Chebyshev response with a center frequency of 200 MHz and a static equal-ripple bandwidth of $\mathrm{BW}_r = 30$ MHz. By the design guidelines, the required $f_m$ would be approximately 30 MHz. The filter specifications are chosen according to the availability of the modulating voltage sources.

Fig. 9 shows the evolution of the filter schematic from an ideal design [see Fig. 9(a)] to a physical implementation using lumped components [see Fig. 9(c) and (d)]. Each ideal admittance inverter between the resonators is implemented by three capacitors arranged in a Π topology [see Fig. 9(b)] [1]. The inverters facing the source and the load impedances are implemented by capacitive dividers/transformers. All the shunt capacitors are absorbed into the resonators, resulting in unequal capacitance of the three resonators. Note that the capacitive networks are narrowband approximations of the ideal inverters. However, since most of the signal power is

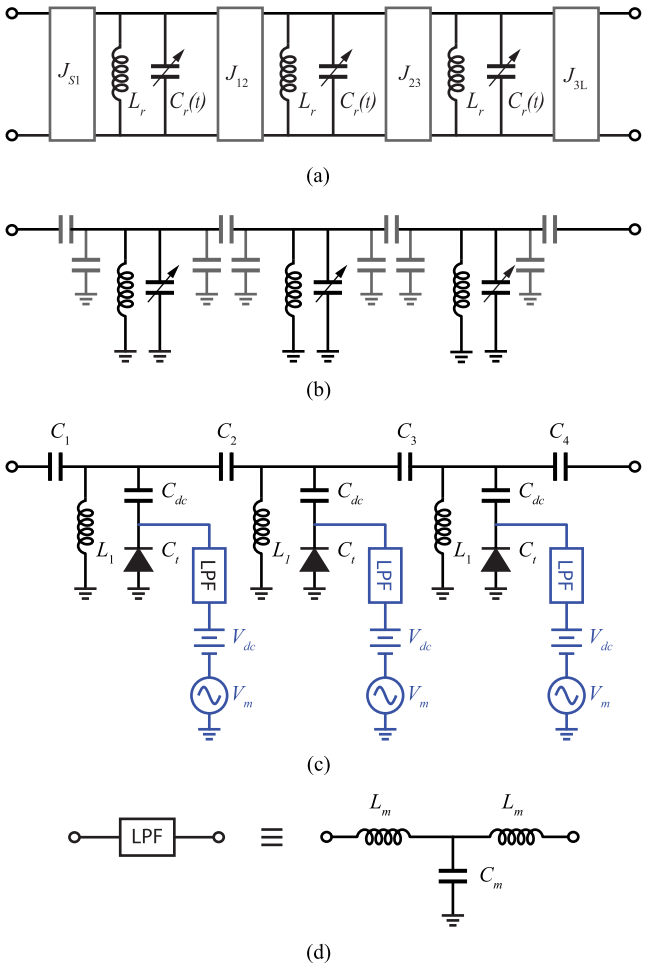


Fig. 9. (a) Circuit topology of the three-pole isolating filter. (b) *LC* implementation of the three-pole isolating filter. (c) Practical circuit implementation of the three-pole isolating filter with varactors. (d) Bias LPF circuit.

contained within $f_0 \pm 3f_m$, where $f_m$ is approximately the filter bandwidth, this approximation does not result in the significant degradation of performance.

The ideal time-varying capacitors in [see Fig. 9(b)] are implemented by reverse-biased varactor diodes. To provide the modulation voltage on the varactors, a dc-blocking capacitor $C_{\rm dc}$ is connected in series with the varactor to isolate the shunt inductor from the dc path. The series capacitors of the admittance inverter also serve to isolate the modulation signal $f_m$ from leakage to RF ports. A bias voltage $V_{\rm dc}$ is provided to each varactor to set the nominal capacitance value. A modulation voltage $V_m$ is provided to each varactor with a constant phase shift $\Delta\phi$ between the varactors. $V_m$ is introduced through a low-pass filter (LPF) to further isolate $f_m$ from $f_0$.

The physical design of the filter is carried out on a 62-mil FR-4 substrate. The dielectric loss of the FR-4 substrate is not a significant concern in this design due to the relatively low center frequency of 200 MHz. The values and part information of the filter components are listed in Table I. In the design of the filter, realistic models from the component vendors are used to simulate and optimize the filter performance.

TABLE I
LIST OF THREE-POLE ISOLATING FILTER DESIGN PARAMETERS

| Parameters | | Value | Part # |
|---|---|---|---|
| Ideal Filter | $f_0$ | 200 MHz | – |
| | Ripple | 0.043 dB | – |
| | $BW_r$ | 30 MHz | – |
| | $BW_{3dB}$ | 46 MHz | – |
| | $L_r$ | 47 nH | – |
| | $C_r$ | 13.2 pF | – |
| | $J_{S1}\&J_{3L}$ | 0.0077 | – |
| | $J_{12}\&J_{23}$ | 0.0026 | – |
| | $\xi$ | 0.25 | – |
| | $\Delta\phi$ | 45° | – |
| Implementation | $L_1\&L_3$ | 47 nH | 1111SQ-47N (Coilcraft) |
| | $L_2$ | 68 nH | 1515SQ-68N (Coilcraft) |
| | $C_{dc}$ | 82 pF | 251R14S820JV4S (Johanson) |
| | $C_t$ | 3.8–27 pF | SMV1236 (Skyworks) |
| | $C_1\&C_4$ | 8.2 pF | 1111N8R3BW501 (PPI) |
| | $C_2\&C_3$ | 2.4 pF | 1111N2R4BW501 (PPI) |
| | $L_m$ | 180 pH | 2222SQ-181 (Coilcraft) |
| | $C_m$ | 82 pF | 251R14S820JV4S (Johanson) |
| | $f_m$ | 30 MHz | – |
| | $\Delta\phi$ | 70° | – |

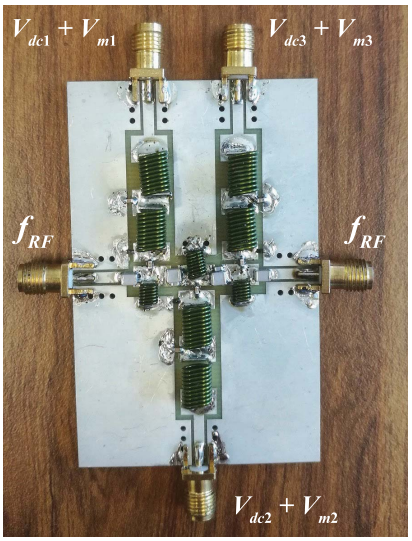


Fig. 10. Photograph of the fabricated lumped-element three-pole isolating filter.

For example, the parasitics of the SMV1236 varactors (equivalent series resistance $R_s = 0.56\ \Omega$ and series inductance $L_s = 0.7$ nH) are included in the simulations. Fig. 10 shows a photograph of the fabricated filter.

The measurement setup is shown in Fig. 11. Two dual-channel function generators (Rigol DG5252) are used to supply the modulation voltage $V_m$ with dc offset $V_{\rm dc}$ to the three varactors. A Rigol DS1102E oscilloscope is used to monitor the amplitude and the phase of the modulation

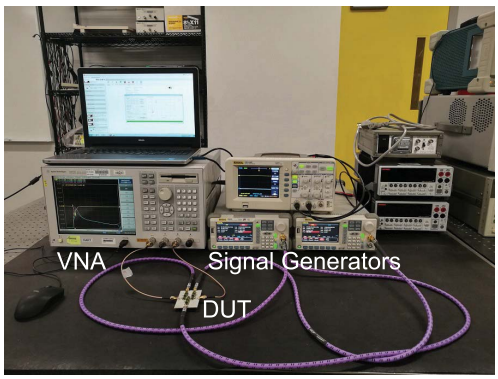


Fig. 11. Experimental demonstration of the isolating BPF.

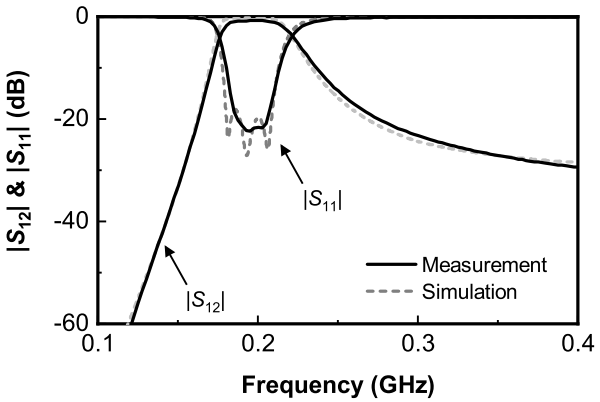


Fig. 12. Simulated and measured nonmodulated results.

voltages. The RF performance is measured with the Agilent vector network analyzer E5071A.

Fig. 12 shows the simulated and measured S-parameters when there is no STM. The reverse-biased dc voltages on the three varactors are 5.0, 4.7, and 5.0 V, which gives the equivalent static capacitances of 6, 6.3, and 6.0 pF, respectively. It should be noted that the static capacitance of the middle resonator is larger than that of the side resonators to compensate for the absorbed larger negative capacitors in Fig. 9, which well illustrates the evolution of the filter implementation from an ideal design. The static filter exhibits an equal-ripple bandwidth of 29 MHz, a 3-dB bandwidth of 45 MHz (175–220 MHz), and a minimum insertion loss of 0.8 dB. The measurement agrees very well with the simulated dates.

Fig. 13 shows the filter response when STM is introduced. In the measurement, the modulation frequency $f_m$ is set to 28 MHz. As predicted by the studies presented in Section II, $f_m$ is very close to the equal-ripple bandwidth of the filter. The modulation voltages applied on the varactors are 2.4, 2.3, and 2.4 V, corresponding to a capacitance variation of 5.0–10 pF. The modulation phase difference $\Delta\phi$ between the adjacent sources is found to be 45°.

Fig. 13(a) and (b) shows the measured forward transmission $S_{21}$ and backward $S_{12}$ in comparison with the simulation. The filter has a very good forward filtering response with a minimum passband insertion loss of 1 dB in simulation and 1.5 dB in measurement. The measured 3-dB bandwidth covers

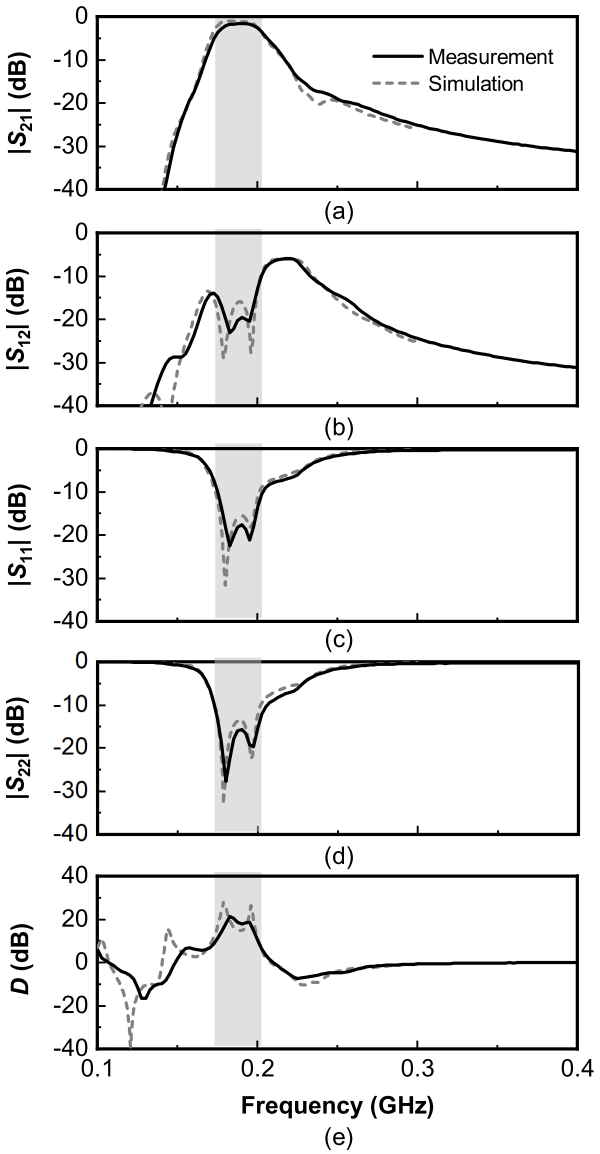


Fig. 13. Simulated and measured modulated responses. (a) Insertion loss $|S_{21}|$. (b) Reverse isolation $|S_{12}|$. (c) Reflection $|S_{11}|$. (d) Reflection $|S_{22}|$. (e) Directivity $D$.

the frequency range of 170–203 MHz, which is slightly smaller than the nonmodulated case. Backward $S_{12}$ of the filter has two zeros in the filter's passband, resulting in a directivity $D$ better than 20 dB in the passband [see Fig. 13(e)]. The power in the backward direction is spread to all the IM frequencies that are located in the stopband of the filter; most of the converted IM frequencies will be reflected back to port 2. $S_{12}$ in the lower stopband is lower than $-15$ dB, and it almost goes up to $-8$ dB, differing from the theoretical analysis, which is all bellow $-10$ dB. It is due to the approximate implementation of an ideal frequency-independent coupling (J-inverter), i.e., frequency-dependent capacitive coupling (capacitor). The filter is well matched at both ports, showing better than 15 dB of return loss. In all cases, the measurement agrees very well with simulation, validating the effectiveness of the design theory and strategies presented in this paper.

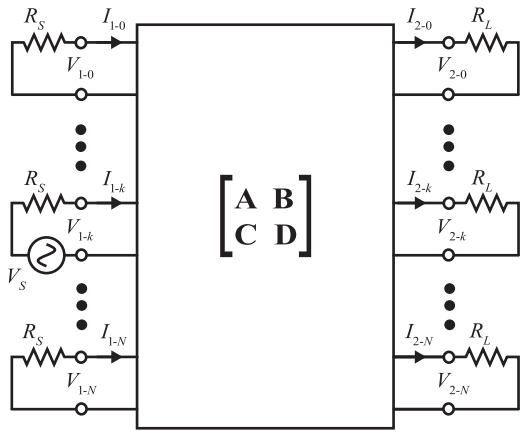


Fig. 14. General multimode circuit with excitation at $k$th mode at port 1.

## V. Conclusion

In this paper, we have demonstrated a novel isolating BPF with low-loss forward transmission and high reverse isolation, thus realizing the functions of a BPF and an isolator in one device. The nonreciprocal response is created by modulating the resonators of the filter with an appropriate modulation frequency, modulation index, and phase difference. A spectral domain analysis method is developed to understand the behavior of the circuit. Using this theory, we show that the nonreciprocal frequency conversion due to the modulated resonators is responsible for creating the in-band (same-frequency) nonreciprocity. An isolating BPF example has been demonstrated at a center frequency of 200 MHz with a forward insertion loss of 1.5 dB and a reverse isolation of 20 dB over a bandwidth of 28 MHz. The study presented in this paper opens doors to many interesting nonreciprocal devices and phenomena in the RF and microwave frequency range.

## Appendix

The general multimode circuit is given in Fig. 14, where there are $N$ modes at both port 1 and port 2, and an excitation of the $k$th mode is connected to the circuit with source impedance $R_S$, while all the other modes at port 1 are terminated with impedance $R_S$ and all modes at port 2 are terminated with impedance $R_L$

$$\begin{bmatrix} \boldsymbol{V_1^k} \\ \boldsymbol{I_1^k} \end{bmatrix} = \begin{bmatrix} \mathbf{A} & \mathbf{B} \\ \mathbf{C} & \mathbf{D} \end{bmatrix} \begin{bmatrix} \boldsymbol{V_2^k} \\ \boldsymbol{I_2^k} \end{bmatrix} \tag{17}$$

where $\boldsymbol{V_1^k}$, $\boldsymbol{I_1^k}$, and $\boldsymbol{V_2^k}$, $\boldsymbol{I_2^k}$ are spectral vectors at port 1 and port 2, respectively, and the superscript letter $k$ of the ABCD network matrix represents the excitation at $k$th mode, where $k = 0, 1, \ldots, N$. In (17), **A**, **B**, **C**, and **D** are the submatrices of the network matrix **ABCD**.

Imposing the boundary conditions, we have

$$\boldsymbol{V_S^k} = \boldsymbol{I_1^k} R_S + \boldsymbol{V_1^k} \tag{18a}$$

$$\boldsymbol{V_2^k} = \boldsymbol{I_2^k} R_L \tag{18b}$$

where $R_S$ and $R_L$ are the time-invariant impedance at port 1 and port 2, respectively. $\boldsymbol{V_S^k} = [\ldots, 0, 0, V_S, 0, 0, \ldots]^T$ is a vector whose only nonzero value corresponds to the excitation mode voltage.

From (17) and (18), the following equations can be derived:

$$\boldsymbol{V_S^k} = [\mathbf{U} + (\mathbf{A}R_L + \mathbf{B})(\mathbf{C}R_S R_L + \mathbf{D}R_S)^{-1}]R_S \boldsymbol{I_1^k} \tag{19a}$$

$$\boldsymbol{V_S^k} = (\mathbf{A} + \mathbf{B}/R_L + \mathbf{C}R_S + \mathbf{D}R_S/R_L)\boldsymbol{V_2^k}. \tag{19b}$$

Next, we normalize (19) with the excitation mode voltage $V_S$, obtaining

$$\overline{\boldsymbol{V_S^k}} = [\mathbf{U} + (\mathbf{A}R_L + \mathbf{B})(\mathbf{C}R_S R_L + \mathbf{D}R_S)^{-1}]R_S(\boldsymbol{I_1^k}/V_S) \tag{20a}$$

$$\overline{\boldsymbol{V_S^k}} = (\mathbf{A} + \mathbf{B}/R_L + \mathbf{C}R_S + \mathbf{D}R_S/R_L)(\boldsymbol{V_2^k}/V_S) \tag{20b}$$

where $\overline{\boldsymbol{V_S^k}} = [\ldots, 0, 0, 1, 0, 0, \ldots]^T$ with only one nonzero value for the $k$th element, which identifies the source position. The S-parameters can be written as

$$\boldsymbol{S_{11}^k} = \overline{\boldsymbol{V_S^k}} - 2[\mathbf{U} + (\mathbf{A}R_L + \mathbf{B})(\mathbf{C}R_S R_L + \mathbf{D}R_S)^{-1}]^{-1} \tag{21a}$$

$$\boldsymbol{S_{21}^k} = 2\sqrt{R_L/R_S}(\mathbf{A} + \mathbf{B}/R_L + \mathbf{C}R_S + \mathbf{D}R_S/R_L)^{-1} \tag{21b}$$

where $\boldsymbol{S_{11}^k}$ is a vector with each element corresponding to the reflection at different modes at port 1 when the excitation is located at the $k$th mode at port 1 and $\boldsymbol{S_{21}^k}$ is a vector with each element corresponding to the transmission at different modes at port 2 when the excitation is located at the $k$th mode at port 1.

Then, the spectral **S**-parameter for the multiple-mode circuit is defined as

$$\mathbf{S_{11}} = \left[\boldsymbol{S_{11}^0}, \ldots, \boldsymbol{S_{11}^k}, \ldots, \boldsymbol{S_{11}^N}\right] \tag{22a}$$

$$\mathbf{S_{21}} = \left[\boldsymbol{S_{21}^0}, \ldots, \boldsymbol{S_{21}^k}, \ldots, \boldsymbol{S_{21}^N}\right]. \tag{22b}$$

Substituting (21) into (22) yields

$$\mathbf{S_{11}} = \mathbf{U} - 2[\mathbf{U} + (\mathbf{A}R_L + \mathbf{B})(\mathbf{C}R_S R_L + \mathbf{D}R_S)^{-1}]^{-1} \tag{23a}$$

$$\mathbf{S_{21}} = 2\sqrt{\frac{R_S}{R_L}}[\mathbf{A} + \mathbf{B}/R_L + \mathbf{C}R_S + \mathbf{D}R_S/R_L]^{-1}. \tag{23b}$$

Following the same procedure, the spectral **S**-parameters $\mathbf{S_{22}}$ and $\mathbf{S_{12}}$ can be derived as

$$\mathbf{S_{22}} = \mathbf{U} - 2[\mathbf{U} + (\mathbf{A}R_L + \mathbf{C}R_S R_L)^{-1}(\mathbf{B} + \mathbf{D}R_S)]^{-1} \tag{24}$$

$$\mathbf{S_{12}} = 2[\mathbf{U} + (\mathbf{A}R_L + \mathbf{B})(\mathbf{C}R_L + \mathbf{D})^{-1}/R_S]^{-1} \times [\mathbf{A} - (\mathbf{A}R_L + \mathbf{B})(\mathbf{C}R_L + \mathbf{D})^{-1}\mathbf{C}]. \tag{25}$$

Thus, the spectral **S**-parameter matrix for the multiple-mode circuit is derived. For the conventional dual-port network under single-mode situation ($N = 1$), the S-parameter matrix in (24) and (25) becomes

$$S_{11} = \frac{A + B/R_L - CR_S - DR_S/R_L}{A + B/R_L + CR_S + DR_S/R_L} \tag{26a}$$

$$S_{21} = \frac{2}{A + B/R_L + CR_S + DR_S/R_L} \tag{26b}$$

$$S_{22} = \frac{-A + B/R_L - CR_S + DR_S/R_L}{A + B/R_L + CR_S + DR_S/R_L} \tag{26c}$$

$$S_{12} = \frac{2(AD - BC)}{AR_L/R_S + B/R_S + CR_L + D} \tag{26d}$$

which is exactly the same as given in [1].

## REFERENCES


[1] D. M. Pozar, *Microwave Engineering*. Hoboken, NJ, USA: Wiley, 2012.

[2] D. Bharadia, E. McMilin, and S. Katti, "Full duplex radios," in *Proc. ACM SIGCOMM Conf.*, Aug. 2013, pp. 375–386.

[3] J. Zhou *et al.*, "Integrated full duplex radios," *IEEE Commun. Mag.*, vol. 55, no. 4, pp. 142–151, Apr. 2017.

[4] N. Reiskarimian, M. B. Dastjerdi, J. Zhou, and H. Krishnaswamy, "Analysis and design of commutation-based circulator-receivers for integrated full-duplex wireless," *IEEE J. Solid-State Circuits*, vol. 53, no. 8, pp. 2190–2201, Aug. 2018.

[5] A. Kord, D. L. Sounas, and A. Alù, "Achieving full-duplex communication: Magnetless parametric circulators for full-duplex communication systems," *IEEE Microw. Mag.*, vol. 19, no. 1, pp. 84–90, Jan./Feb. 2018.

[6] C. Caloz, A. Alù, S. Tretyakov, D. Sounas, K. Achouri, and Z.-L. Deck-Léger, "Electromagnetic nonreciprocity," *Phys. Rev. Appl.*, vol. 10, Oct. 2018, Art. no. 047001. doi: 10.1103/PhysRevApplied.10.047001.

[7] C. E. Fay and R. L. Comstock, "Operation of the ferrite junction circulator," *IEEE Trans. Microw. Theory Techn.*, vol. MTT-13, no. 1, pp. 15–27, Jan. 1965.

[8] C. K. Seewald and J. R. Bray, "Ferrite-filled antisymmetrically biased rectangular waveguide isolator using magnetostatic surface wave modes," *IEEE Trans. Microw. Theory Techn.*, vol. 58, no. 6, pp. 1493–1501, Jun. 2010.

[9] D. R. Taft, G. R. Harrison, and L. R. Hodges, "Millimeter resonance isolators utilizing hexagonal ferrites," *IEEE Trans. Microw. Theory Techn.*, vol. MTT-11, no. 5, pp. 346–356, Sep. 1963.

[10] Y. Konishi, "Lumped element circulators," *IEEE Trans. Magn.*, vol. MAG-11, no. 5, pp. 1262–1266, Sep. 1975.

[11] S. A. Oliver *et al.*, "Integrated self-biased hexaferrite microstrip circulators for millimeter-wavelength applications," *IEEE Trans. Microw. Theory Techn.*, vol. 49, no. 2, pp. 385–387, Feb. 2001.

[12] S. Tanaka, N. Shimomura, and K. Ohtake, "Active circulators: The realization of circulators using transistors," *Proc. IEEE*, vol. 53, no. 3, pp. 260–267, Mar. 1965.

[13] Y. Ayasli, "Field effect transistor circulators," *IEEE Trans. Magn.*, vol. 25, no. 5, pp. 3242–3247, Sep. 1989.

[14] J.-F. Chang, J.-C. Kao, Y.-H. Lin, and H. Wang, "Design and analysis of 24-GHz active isolator and quasi-circulator," *IEEE Trans. Microw. Theory Techn.*, vol. 63, no. 8, pp. 2638–2649, Aug. 2015.

[15] T. Kodera, D. L. Sounas, and C. Caloz, "Magnetless nonreciprocal metamaterial (MNM) technology: Application to microwave components," *IEEE Trans. Microw. Theory Techn.*, vol. 61, no. 3, pp. 1030–1042, Mar. 2013.

[16] G. Carchon and B. Nauwelaers, "Power and noise limitations of active circulators," *IEEE Trans. Microw. Theory Techn.*, vol. 48, no. 2, pp. 316–319, Feb. 2000.

[17] D. L. Sounas, J. Soric, and A. Alù, "Broadband passive isolators based on coupled nonlinear resonances," *Nature Electron.*, vol. 1, no. 2, pp. 113–119, Feb. 2018.

[18] Z. Yu and S. Fan, "Complete optical isolation created by indirect interband photonic transitions," *Nature Photon.*, vol. 3, no. 2, pp. 91–94, Feb. 2009.

[19] H. Lira, Z. Yu, S. Fan, and M. Lipson, "Electrically driven nonreciprocity induced by interband photonic transition on a silicon chip," *Phys. Rev. Lett.*, vol. 109, no. 3, 2012, Art. no. 033901.

[20] D. Correas-Serrano, J. S. Gomez-Diaz, D. L. Sounas, Y. Hadad, A. Alvarez-Melcon, and A. Alù, "Nonreciprocal graphene devices and antennas based on spatiotemporal modulation," *IEEE Antennas Wireless Propag. Lett.*, vol. 15, pp. 1529–1532, 2016.

[21] S. Qin, Q. Xu, and Y. E. Wang, "Nonreciprocal components with distributedly modulated capacitors," *IEEE Trans. Microw. Theory Techn.*, vol. 62, no. 10, pp. 2260–2272, Oct. 2014.

[22] R. Fleury *et al.*, "Sound isolation and giant linear nonreciprocity in a compact acoustic circulator," *Science*, vol. 343, pp. 516–519, Jan. 2014.

[23] D. L. Sounas, C. Caloz, and A. Alù, "Giant non-reciprocity at the subwavelength scale using angular momentum-biased metamaterials," *Nature Commun.*, vol. 4, Sep. 2013, Art. no. 2407.

[24] N. A. Estep, D. L. Sounas, J. Soric, and A. Alù, "Magnetic-free non-reciprocity and isolation based on parametrically modulated coupled-resonator loops," *Nature Phys.*, vol. 10, no. 12, pp. 923–927, Dec. 2014.

[25] N. A. Estep, D. L. Sounas, and A. Alù, "Magnetless microwave circulators based on spatiotemporally modulated rings of coupled resonators," *IEEE Trans. Microw. Theory Techn.*, vol. 64, no. 2, pp. 502–518, Feb. 2016.

[26] A. Kord, D. L. Sounas, and A. Alù, "Magnet-less circulators based on spatiotemporal modulation of bandstop filters in a delta topology," *IEEE Trans. Microw. Theory Techn.*, vol. 66, no. 2, pp. 911–926, Feb. 2018.

[27] M. M. Torunbalci, T. J. Odelberg, S. Sridaran, R. C. Ruby, and S. A. Bhave, "An FBAR circulator," *IEEE Microw. Wireless Compon. Lett.*, vol. 28, no. 5, pp. 395–397, May 2018.

[28] C. Xu, E. Calayir, and G. Piazza, "Magnetic-free electrical circulator based on AlN MEMS filters and CMOS RF switches," in *Proc. Micro Electro Mech. Syst. (MEMS)*, Jan. 2018, pp. 755–758.

[29] A. Kord, D. L. Sounas, and A. Alù, "Pseudo-linear time-invariant magnetless circulators based on differential spatiotemporal modulation of resonant junctions," *IEEE Trans. Microw. Theory Techn.*, vol. 66, no. 6, pp. 2731–2745, Jun. 2018.

[30] Y. Yu *et al.*, "Magnetic-free radio frequency circulator based on spatiotemporal commutation of MEMS resonators," in *Proc. IEEE Micro Electro Mech. Syst.*, Jan. 2018, pp. 154–157.

[31] A. Kord, D. L. Sounas, Z. Xiao, and A. Alù, "Broadband cyclic-symmetric magnetless circulators and theoretical bounds on their bandwidth," *IEEE Trans. Microw. Theory Techn.*, vol. 66, no. 12, pp. 5472–5481, Dec. 2018.

[32] M. M. Biedka, R. Zhu, Q. M. Xu, and Y. E. Wang, "Ultra-wide band non-reciprocity through sequentially-switched delay lines," *Sci. Rep.*, vol. 7, Jan. 2017, Art. no. 40014.

[33] N. Reiskarimian and H. Krishnaswamy, "Magnetic-free non-reciprocity based on staggered commutation," *Nature Commun.*, vol. 7, Apr. 2016, Art. no. 11217.

[34] N. Reiskarimian, J. Zhou, and H. Krishnaswamy, "A CMOS passive LPTV nonmagnetic circulator and its application in a full-duplex receiver," *IEEE J. Solid-State Circuits*, vol. 52, no. 5, pp. 1358–1372, May 2017.

[35] A. Nagulu *et al.*, "Nonreciprocal components based on switched transmission lines," *IEEE Trans. Microw. Theory Techn.*, vol. 66, no. 11, pp. 4706–4725, Nov. 2018.

[36] T. Dinc, M. Tymchenko, A. Nagulu, D. Sounas, A. Alù, and H. Krishnaswamy, "Synchronized conductivity modulation to realize broadband lossless magnetic-free non-reciprocity," *Nature Commun.*, vol. 8, Oct. 2017, Art. no. 795.

[37] M. D. Hickle, "Synthesis, design, and fabrication techniques for reconfigurable microwave and millimeter-wave filters," Ph.D. dissertation, School Elect. Comput. Eng., Purdue Univ., West Lafayette, IN, USA, 2016.

[38] C. Kurth, "Steady-state analysis of sinusoidal time-variant networks applied to equivalent circuits for transmission networks," *IEEE Trans. Circuits Syst.*, vol. CS-24, no. 11, pp. 610–624, Nov. 1977.


**Xiaohu Wu** (M'15) was born in Hubei, China, in 1987. He received the B.Eng. degree in information engineering and Ph.D. degree in electromagnetic fields and microwave technology from the South China University of Technology, Guangzhou, China, in 2008 and 2013, respectively. His Ph.D. dissertation concerned the exploration of multimode resonators and their applications to filter design.

From 2013 to 2014, he was an Engineer with the East China Research Institute of Electronic Engineering (ECRIEE), Hefei, China, where he was involved in scalable active arrays. In 2015, he joined the School of Electronic and Information Engineering, Nanjing University of Information Science and Technology, Nanjing, China, as an Assistant Professor. Since 2017, he has been a Post-Doctoral Researcher with the Department of Electrical and Computer Engineering, University of California at Davis, Davis, CA, USA. His current research interests include time-varying nonreciprocal devices and absorptive circuit design.

**Xiaoguang (Leo) Liu** (M'10–SM'16) received the bachelor's degree from Zhejiang University, Hangzhou, China, in 2004, and the Ph.D. degree from Purdue University, West Lafayette, IN, USA, in 2010.

In 2011, he joined the Department of Electrical and Computer Engineering, University of California at Davis, Davis, CA, USA, as an Assistant Professor, and was promoted to an Associate Professor in 2017. At the University of California at Davis, his research group is currently investigating various aspects of cutting-edge high-frequency and high-speed circuit and system designs.

**Mark D. Hickle** (S'11–M'17) received the B.S. degree in electrical engineering from the Missouri University of Science and Technology, Rolla, MO, USA, in 2012, and the Ph.D. degree in electrical and computer engineering from Purdue University, West Lafayette, IN, USA, in 2016.

Since 2017, he has been with BAE Systems, Merrimack, NH, USA. His current research interests include high-performance RF/mixed-signal integrated circuits.

Dr. Hickle was a National Defense Science and Engineering Graduate (NDSEG) Fellow while he was with Purdue University. He was a co-recipient of the First Place Award for the RF-MEMS Tunable Filter Student Design Competitions at the 2014 and 2015 International Microwave Symposium and the First Place Award for the 2015 MTT-S Educational YouTube Video Award.

**Dimitrios Peroulis** (S'99–M'04–SM'15–F'17) received the Ph.D. degree in electrical engineering from the University of Michigan at Ann Arbor, Ann Arbor, MI, USA, in 2003.

He is currently the Reilly Professor of Electrical and Computer Engineering with Purdue University, West Lafayette, IN, USA. He is also the Associate Dean for External Affairs with the College of Engineering. His current research interests include the areas of reconfigurable electronics, cold-plasma RF electronics, and wireless sensors. He has led multiple government and industry programs focused on high-quality-factor reconfigurable systems. He is also co-directing the SMART Films Industry Consortium that includes two dozen groups across ten schools and four colleges. He has coauthored over 380 journal and conference papers.

Dr. Peroulis was the recipient of the National Science Foundation CAREER Award in 2008. He has been inducted into the Book of Great Teachers at Purdue University and has received ten teaching awards, including the 2010 Charles B. Murphy Award, which is Purdue University's highest undergraduate teaching honor. In 2012, he received the Outstanding Paper Award from the IEEE Ultrasonics, Ferroelectrics, and Frequency Control Society (Ferroelectrics Section). In 2014, he was the recipient of the Outstanding Young Engineer Award of the IEEE Microwave Theory and Techniques Society (MTT-S). His students have received numerous student paper/competition awards and research-based scholarships.

**Juan Sebastián Gómez-Díaz** (M'11–SM'16) was born in Ontur, Spain, in 1983. He received the Telecommunications Engineer and Ph.D. degrees in electrical engineering from the Technical University of Cartagena (UPCT), Cartagena, Spain, in 2006 and 2011, respectively.

In 2006, he joined the Telecommunication and Electromagnetic Group (GEAT), UPCT, as a Research Assistant. During the development of his Ph.D., he held visiting research positions with the École Polytechnique de Montréal, Montreal, QC, Canada, and the Fraunhofer Institute for High Frequency Physics and Radar Techniques, Germany. From 2011 to 2014, he was a Post-Doctoral Fellow with the École Polytechnique Fédérale de Lausanne (EPFL), Lausanne, Switzerland. From 2014 to 2016, he continued his post-doctoral work with the Metamaterials and Plasmonic Research Laboratory, The University of Texas at Austin, Austin, TX, USA. He is currently an Assistant Professor with the Electrical and Computer Engineering Department, University of California at Davis, Davis, CA, USA. His current research interests include multidisciplinary areas of electromagnetic wave propagation and radiation, metamaterials and metasurfaces, plasmonics, 2-D materials, nonreciprocal and nonlinear phenomena, and other emerging topics on applied electromagnetics and nanotechnology.

Dr. Gómez-Díaz was a recipient of the Best Ph.D. Thesis Award from the Technical University of Cartagena, the Colegio Oficial de Ingenieros de Telecomunicación (COIT/AEIT) Award to the Best Spanish Ph.D. Thesis in basic information and communication technologies in 2011, the FP7 Marie Curie Fellowship from the European Commision in 2012, the Raj Mittra Award from the 2015 IEEE Antennas and Propagation Society, the Young Scientist Award of the 2015 URSI Atlantic RadioScience Conference, the 2017 Leopold Felsen Award for Excellence in Electrodynamics, and the 2018 NSF CAREER Award. He serves as a Reviewer for several journals on antennas, microwaves/THz, and physics.

**Alejandro Álvarez Melcón** (M'99–SM'07) was born in Madrid, Spain, in 1965. He received the Telecommunications Engineer degree from the Technical University of Madrid (UPM), Madrid, Spain, in 1991, and the Ph.D. degree in electrical engineering from the Swiss Federal Institute of Technology, Lausanne, Switzerland, in 1998.

In 1988, he joined the Signal, Systems and Radiocommunications Department, UPM, as a Research Student, where he was involved in the design, testing, and measurement of broadband spiral antennas for electromagnetic measurements support (EMS) equipment. From 1991 to 1993, he was with the Radio Frequency Systems Division, European Space Agency (ESA/ESTEC), Noordwijk, The Netherlands, where he was involved in the development of analytical and numerical tools for the study of waveguide discontinuities, planar transmission lines, and microwave filters. From 1993 to 1995, he was with the Space Division, Alcatel Espacio Industries, Madrid, and was also with ESA, where he collaborated in several ESA/European Space Research and Technology Centre (ESTEC) contracts. From 1995 to 1999, he was with the Swiss Federal Institute of Technology, École Polytechnique Fédérale de Lausanne (EPFL), Lausanne, where he was involved in the field of microstrip antennas and printed circuits for space applications. In 2000, he joined the Technical University of Cartagena, Cartagena, Spain, where he is currently developing his teaching and research activities.

Dr. Álvarez Melcón was a recipient of the *Journées Internationales de Nice Sur les Antennes* (JINA) Best Paper Award for the best contribution to the JINA'98 International Symposium on Antennas and the Colegio Oficial de Ingenieros de Telecomunicación (COIT/AEIT) Award for the best Ph.D. dissertation in basic information and communication technologies.